Pore Structure Modulation in Kirigamic Zeolitic Imidazolate Framework

Joohan Nam[1], Eunji Jin[2], Leila Abylgazina[2], Jürgen Getzschmann[2], Wen-Long Xue[3], Hong Kyu Lee[1], Hyunchul Oh[1], Hoi Ri Moon[4], Sebastian Henke[3], Andreas Schneemann[*,2], and Wonyoung Choe[**,1,5,6,7]

[1]Department of Chemistry, Ulsan National Institute of Science and Technology (UNIST), Ulsan 44919, Republic of Korea.

[2]Inorganic Chemistry I, Technical University Dresden, Bergstr. 66, 01069 Dresden, Germany.

[3]Anorganische Chemie, Fakultät für Chemie und Chemische Biologie, Technische Universität Dortmund, 44227 Dortmund, Germany.

[4]Department of Chemistry and Nanoscience, Ewha Womans University, 52 Ewhayeodae-gil, Seoul 03760, Republic of Korea.

[5]Graduate School of Carbon Neutrality, Ulsan National Institute of Science and Technology (UNIST), Ulsan 44919, Republic of Korea.

[6]Graduate School of Artificial Intelligence, Ulsan National Institute of Science and Technology (UNIST), Ulsan 44919, Republic of Korea.

[7]Lead Contact

Correspondence: [*]andreas.schneemann@tu-dresden.de, [**]choe@unist.ac.kr

https://doi.org/10.26434/chemrxiv-2024-ffwgh-v2 **ORCID:** https://orcid.org/0000-0001-5123-418X Content not peer-reviewed by ChemRxiv. **License:** CC BY-NC 4.0

KEYWORDS:

Kirigami, Mechanical Metamaterials, Mechanical Properties, Adsorptive Properties, Pore Dimensionality, Zeolitic Imidazolate Frameworks, Metal–Organic Frameworks

https://doi.org/10.26434/chemrxiv-2024-ffwgh-v2 **ORCID:** https://orcid.org/0000-0001-5123-418X Content not peer-reviewed by ChemRxiv. **License:** CC BY-NC 4.0

SUMMARY

Paper crafts, such as origami and kirigami, have become an interdisciplinary research theme transportable from art to science, and further to engineering. Kirigami-inspired architectural design strategies allow the establishment of three-dimensional (3D) mechanical linkages with unprecedented mechanical properties. Herein, we report a crystalline zeolitic imidazolate framework (ZIF), displaying folding mechanics based on a kirigami tessellation, originated from the double-corrugation surface (DCS) pattern. Pressure- and guest-induced responses demonstrate the kirigami mechanism of the ZIF, wherein imidazolate linkers act as hinges, controlling pore dimensionality, resembling the check valve-adapted mechanical manifold. This discovery of the kirigami tessellation inside a flexible ZIF reveals foldable mechanics at the molecular level.

https://doi.org/10.26434/chemrxiv-2024-ffwgh-v2 **ORCID:** https://orcid.org/0000-0001-5123-418X Content not peer-reviewed by ChemRxiv. **License:** CC BY-NC 4.0

INTRODUCTION

Kirigami, an extended version of origami allowing cuts, has moved beyond its conventional usages as craft activities.[1] Recently the kirigamic design principles have extended to mechanical engineering,[2] making it possible to create highly deformable 3D structures with mechanical functionalities.[3–5] These structural features have led to the advances in programmable mechanical metamaterials[6–9] applicable to electronics-free robots,[10] pressure sensors,[11] antennas,[12] electronic devices,[13] and metasurfaces.[14] Kirigami tessellations, composed of embedded patterns are the key features for these recent applications, as exemplified by a two-dimensional (2D) molecular framework based on an origami tessellation (Figure 1A, Table S1).[15–23] Despite the advent of various foldable materials, however, developing 3D folding solid-state structures remains an important challenge at the nano- and molecular scale.[24]

To create a solid-state kirigami, we envisioned that ZIFs,[25–27] a subclass of metal−organic frameworks (MOFs) with zeolitic topologies, are an ideal platform, due to their highly deformable nature under various stimuli.[28] Notably, tetrahedral Zn metal centers can act as pivoting points, resulting in unique mechanical properties in contrast to zeolites.[29–32]

Here, we report a kirigamic characteristics of **gis**-ZIF-1,[29] composed of 4-membered rings (4MRs) acting as rigid tiles. By connecting Zn sites, we unveiled the kirigami tessellation in the ZIF, derived from origami tessellations observed in DCS and square twist patterns (Figure 1B).[33] The mechanical response of **gis**-ZIF-1 exhibits the folding mechanics, analogous to kirigami movement in the solid-state. The mechanics can also be controlled by solvents, wherein the tetragonal large pore (*lp*) structure of **gis**-ZIF-1 is transformed to the orthorhombic narrow pore (*np*) structure, confirmed by single-crystal X-ray diffraction (SCXRD). Interestingly, this kirigamic transition accompanies a change in pore structure, similar to a

https://doi.org/10.26434/chemrxiv-2024-ffwgh-v2 **ORCID:** https://orcid.org/0000-0001-5123-418X Content not peer-reviewed by ChemRxiv. **License:** CC BY-NC 4.0

mechanical manifold regulating water flow in a pipe through a check valve. The reversible *np*-to-*lp* transition is also demonstrated by N_2, O_2 and CO_2 adsorption. We anticipate that this kirigami-inspired ZIF will play a significant role as an emerging class of kirigamic mechanical metamaterials and serve as smart adsorbents in the foreseeable future.

https://doi.org/10.26434/chemrxiv-2024-ffwgh-v2 **ORCID:** https://orcid.org/0000-0001-5123-418X Content not peer-reviewed by ChemRxiv. **License:** CC BY-NC 4.0

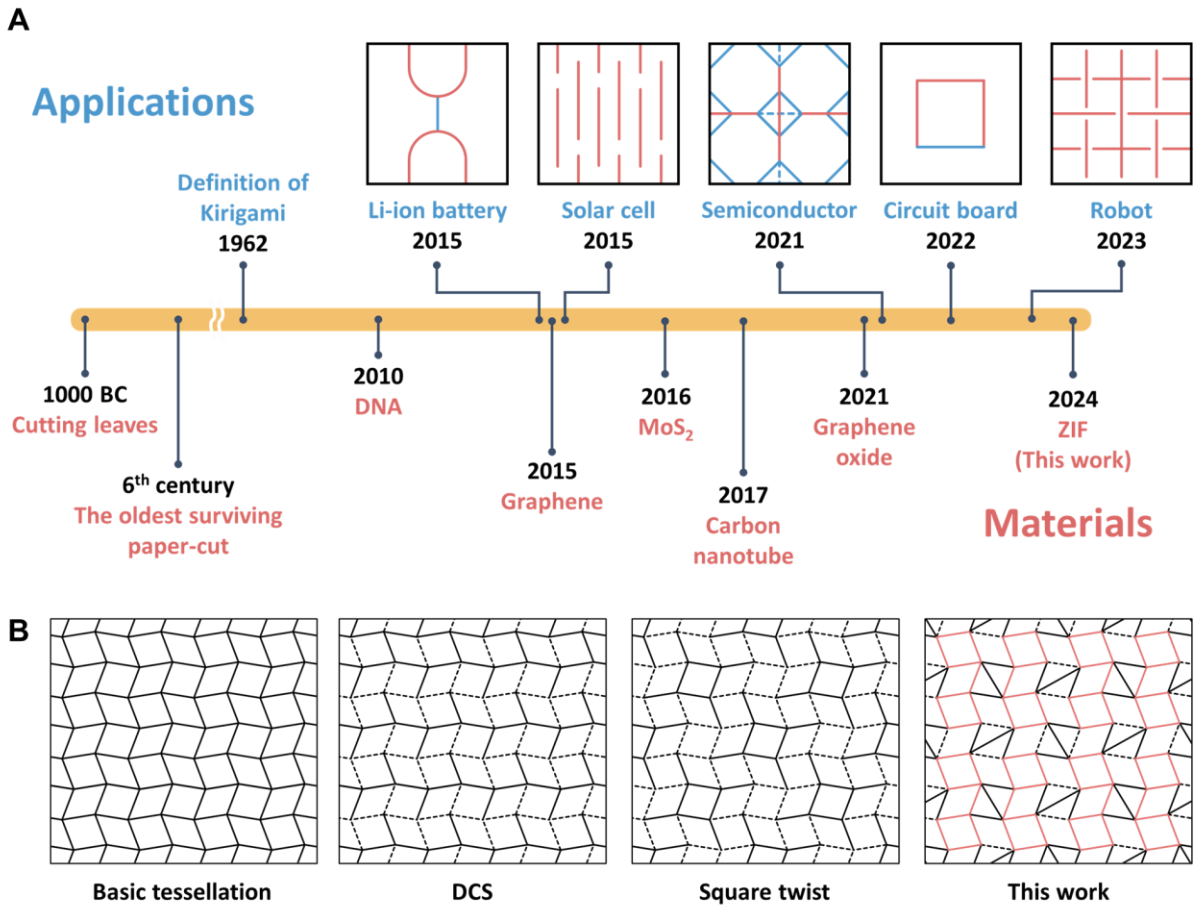

Figure 1. A brief history of the kirigami and the kirigami tessellation of gis-ZIF-1 and related origami tessellations. (A) Applications with related kirigami tessellations, and kirigami-inspired materials (see Table S1). In the figures, blue and red letters represent the applications and materials related to the kirigami. In the tessellations, cutting edges and foldable hinges are represented as red and blue lines, respectively. (B) Comparison between DCS (second from the left) and square (second from the right) twist origami and related kirigami tessellation (right) demonstrated in this work, sharing a same basic tessellation (left) represented by black dotted (valley folding), solid (mountain folding), and red solid (cutting) lines.

https://doi.org/10.26434/chemrxiv-2024-ffwgh-v2 **ORCID:** https://orcid.org/0000-0001-5123-418X Content not peer-reviewed by ChemRxiv. **License:** CC BY-NC 4.0

RESULTS

Synthesis and structural characterization. Synthesis of **gis**-ZIF-1 was conducted according to a synthetic method described in our previous publication,[29] with zinc(II) triflate, imidazole ligands (HIm), and ethylenediamine (EDA) in N,N-diethylformamide (DEF) solvent. The **gis**-ZIF-1 structure consists of tetrahedral Zn^{2+} metal centers and imidazolate (Im) linkers in 1:2 molar ratio, with tetragonal $I4_1/a$ space group. The synchrotron powder X-ray diffraction pattern of the as-synthesized **gis**-ZIF-1 matches well with the Bragg reflections from the reported SCXRD data (Figure S1). We note that the **gis** topology can be represented as interconnected double-crankshaft chains (dcc) with underlying diamond-like connectivity, where the dcc belongs to the periodic building units found in some zeolite topologies, such as **gis**, **gme**, and **mer** (Figure S2).[34] The structure of **gis**-ZIF-1 can also be represented as interconnected dcc units by connecting tetrahedral Zn sites, wherein Im linkers are edges of 4-membered rings (4MRs, or butterfly-shaped flattened tetrahedra) with two different symmetrical positions (Figure 2A). To our surprise, the arrangement of 4MRs in **gis**-ZIF-1 is closely related to that of kirigami tessellation, as can be seen in Figure 2B. Such kirigami tessellation observed in **gis**-ZIF-1 can be derived from the DCS and square twist origami tessellations (Figure 2C, Figure S3).[15] Because these patterns are highly deformable,[33] we expected that **gis**-ZIF-1 might undergo a folding movement when suitable external stimuli (e.g. pressure) were applied.

https://doi.org/10.26434/chemrxiv-2024-ffwgh-v2 **ORCID:** https://orcid.org/0000-0001-5123-418X Content not peer-reviewed by ChemRxiv. **License:** CC BY-NC 4.0

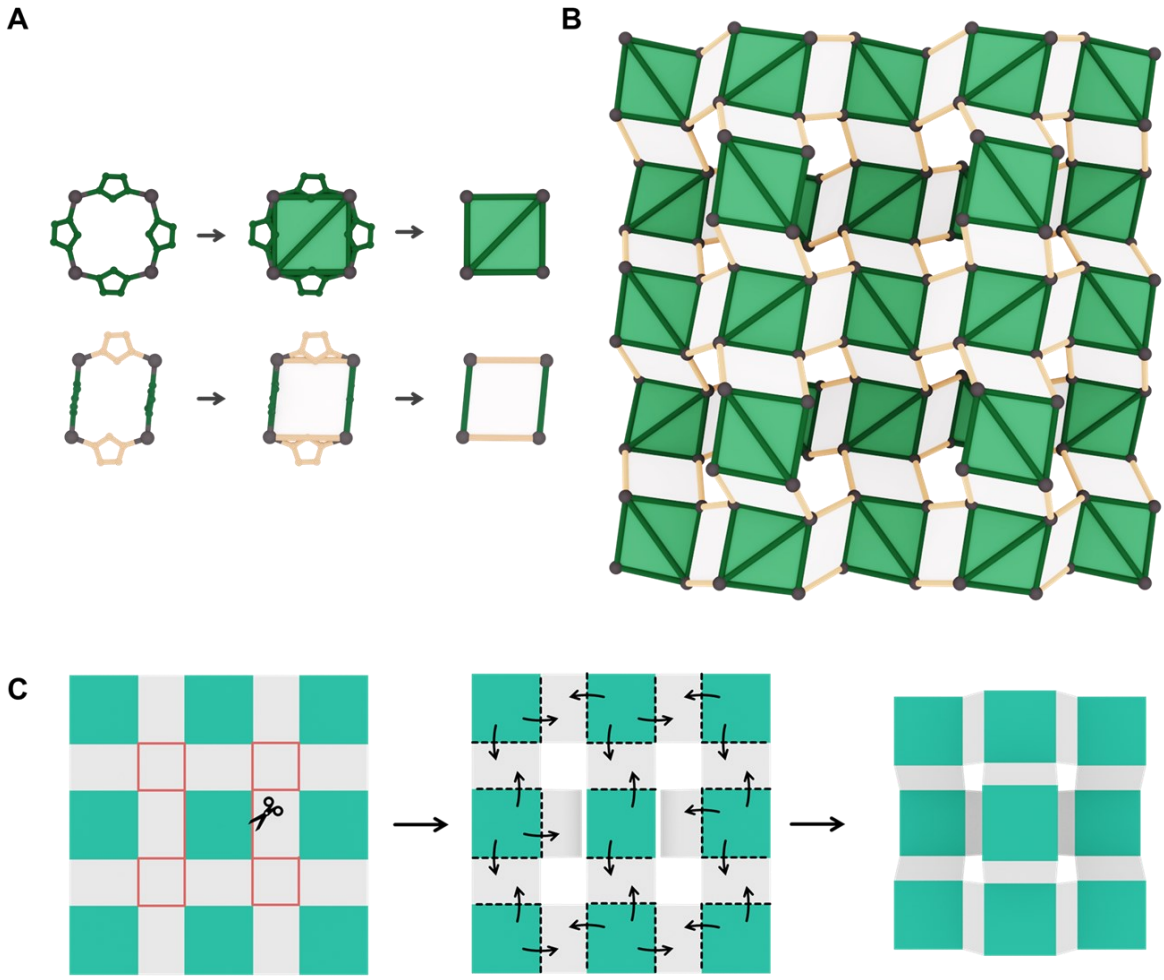

Figure 2. Crystal structure and kirigamic tessellation of gis-ZIF-1. (A) Two 4MR components constructed by two types of imidazolate sites (each site colored by green and light orange). Each imidazolate is connected by Zn atoms (colored by grey), and 4MR components are represented by green and white tiles. The green 4MRs have a butterfly-tetrahedral shape, so the triangular tiles are in contact along the green folding hinges. (B) Simplified tetragonal **gis**-ZIF-1 structure based on kirigami tessellation. (C) Kirigami diagram representing DCS-derived kirigamic tessellation of **gis**-ZIF-1. Resulting paper model corresponds to the unit cell of **gis**-ZIF-1.

https://doi.org/10.26434/chemrxiv-2024-ffwgh-v2 **ORCID:** https://orcid.org/0000-0001-5123-418X Content not peer-reviewed by ChemRxiv. **License:** CC BY-NC 4.0

Mechanical response. To test our hypothesis, we conducted pressure-dependent synchrotron PXRD measurements for **gis**-ZIF-1, over a range of 0 GPa to 0.4 GPa (Figure 3A). Full PXRD profiles (total 29 data points) were fitted by Le Bail method, and all data has R_{wp} values smaller than 3% (Table S2). Over the pressure range, the unit cell volume decreased about 5.4% from 6548.0(5) $Å^3$ to 6197.0(16) $Å^3$. Also, tetrahedron density (the number of Zn sites per cell volume) increased about 5.7% from 2.4 nm^{-3} to 2.6 nm^{-3}. The cell parameters, *a* and *c*, decreased about 1.2% and 3.0%, respectively, implying anisotropic compression. Based on these cell parameters, we calculated mechanical properties such as bulk modulus and compressibility (Figure 3B). The general bulk modulus is 7.5 GPa, similar to those found in other ZIFs.[35,36] Linear and volume compressibility (κ) were also calculated, where the linear compressibility along the *a* and *c* direction (κ_a and κ_c) and volume compressibility (κ_V) are nearly constant, with their average values of 30, 79 and 137 TPa^{-1}, respectively (Figure S4).

For a detailed analysis of these mechanical response, we refined the framework structures from PXRD via the Rietveld method for 5 data points ranging from 0 GPa to 0.4 GPa with 0.1 GPa intervals (Table S3, Figure S5-S9). To check the kirigami model of **gis**-ZIF-1, we evaluated the rigidity of each 4MR tile by tracking distances and angles between Zn sites (Table S4). Notably, Zn-Zn distances (L_1 and L_2) and Zn-Zn-Zn angles are nearly constant over the whole pressure range for each symmetrically identical edge (Figure 3C). When each area of tiles was calculated as S_1 (green tile) and S_2 (white tile), respectively, the changes in S_1 and S_2 are minimal (less than 2%), indicating that 4MR tiles are rather rigid. Mechanical compression of **gis**-ZIF-1 is closely related to the collective motion of these 4MR tiles.

Folding mechanics based on kirigami tessellation. To unveil the actual mechanical movement, we defined folding and rotating angles, which are well-established parameters to explain solid-state mechanics of origami and machine-like MOFs (Figure 3D).[15,29] Considering

https://doi.org/10.26434/chemrxiv-2024-ffwgh-v2 **ORCID:** https://orcid.org/0000-0001-5123-418X Content not peer-reviewed by ChemRxiv. **License:** CC BY-NC 4.0

the crystal symmetry, the **gis**-ZIF-1 structure includes two types of folding angles: angles between green tiles (α) and between green and white tiles (β). Both angles are highly flexible under mechanical stress, where folding angle α and β were decreased about 30.2° and 9°, from 0 GPa to 0.4 GPa, respectively (Figure 3E, Table S5).

Based on these rigid and flexible parameters inside **gis**-ZIF-1, we have built the kirigamic mechanical model (Figure S10).

$$c = 4\sqrt{L_2^2 + \frac{2(1-\cos\alpha)}{3-\cos\alpha}L_1^2\cos 2\theta - \frac{a^2}{4} + L_1\sqrt{\frac{2a^2(1-\cos\alpha)}{3-\cos\alpha}\sin^2\theta - 4\left(\frac{1-\cos\alpha}{3-\cos\alpha}\right)^2 L_1^2\sin^2 2\theta}}$$

In this equation, c parameter (denoted as c) is a function of the folding angle α and the rotating angle θ, while Zn-Zn distances (L_1, L_2) and a parameter (denoted as a) are set as constants. Surprisingly, this model function c matched well with experimental c parameters, as can be seen in Figure 3F. Furthermore, the folding angle α and c parameter are directly related (Figure 3G, Figure S11). The kirigami mechanics based on the structural model follows the experimental crystallographic data, indicating that the folding movement is indeed the origin of the unit cell compression observed (Figure 4).

https://doi.org/10.26434/chemrxiv-2024-ffwgh-v2 **ORCID:** https://orcid.org/0000-0001-5123-418X Content not peer-reviewed by ChemRxiv. **License:** CC BY-NC 4.0

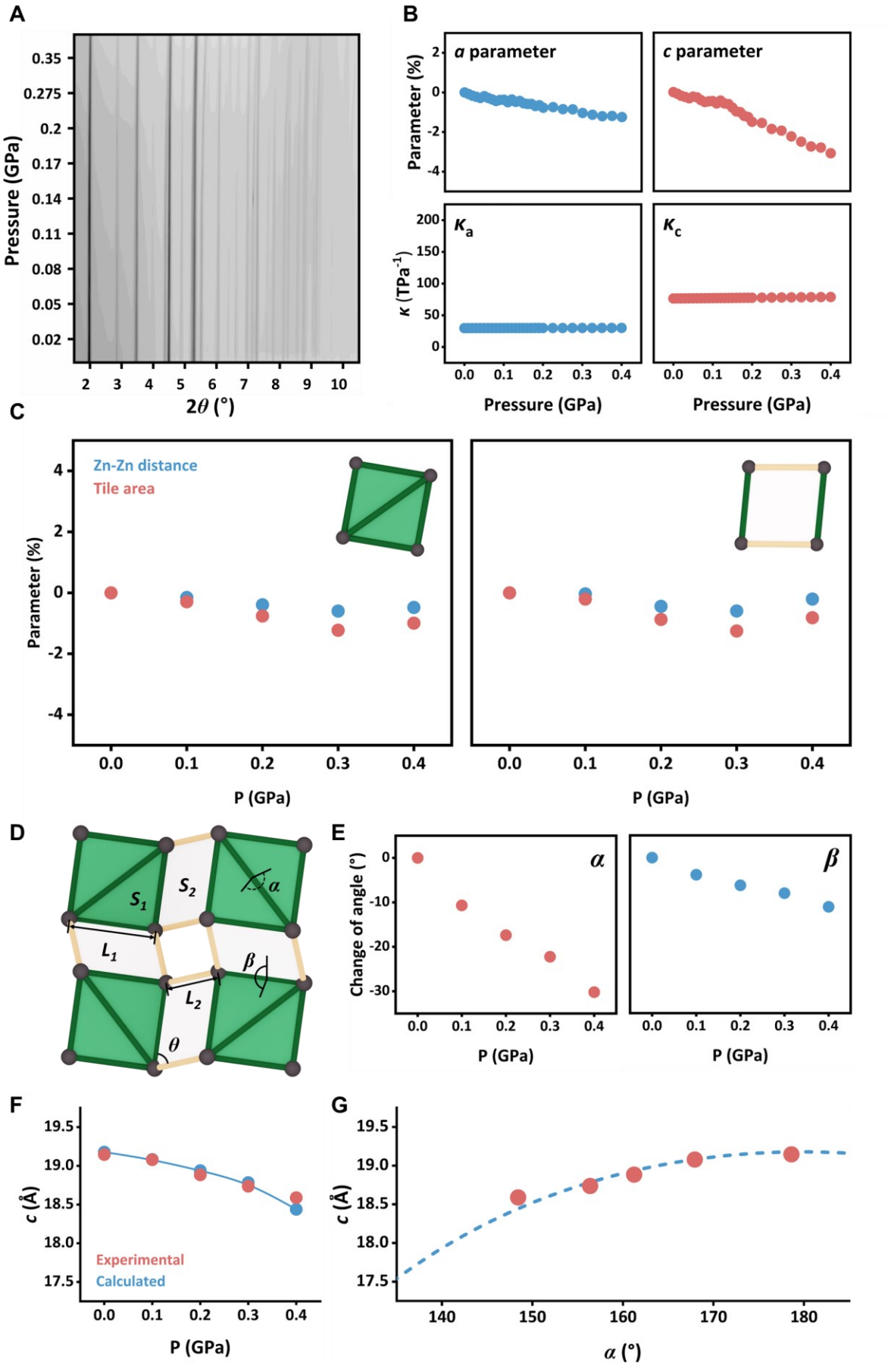

https://doi.org/10.26434/chemrxiv-2024-ffwgh-v2 **ORCID:** https://orcid.org/0000-0001-5123-418X Content not peer-reviewed by ChemRxiv. **License:** CC BY-NC 4.0

Figure 3. Mechanical response of gis-ZIF-1. (A) Pressure-dependent PXRD patterns from 0 to 0.4 GPa. (B) Relative change of cell parameters, and related compressibility. (C) Comparison of the changes in Zn-Zn distances and related area values inside rigid tiles (green and white tile, respectively). (D) 2D projected model and (E) pressure-dependent folding angles inside **gis**-ZIF-1. Comparison of experimental (red) and calculated (blue) (F) *c* parameters and (G) relationship between folding angle α and *c* parameters.

https://doi.org/10.26434/chemrxiv-2024-ffwgh-v2 **ORCID:** https://orcid.org/0000-0001-5123-418X Content not peer-reviewed by ChemRxiv. **License:** CC BY-NC 4.0

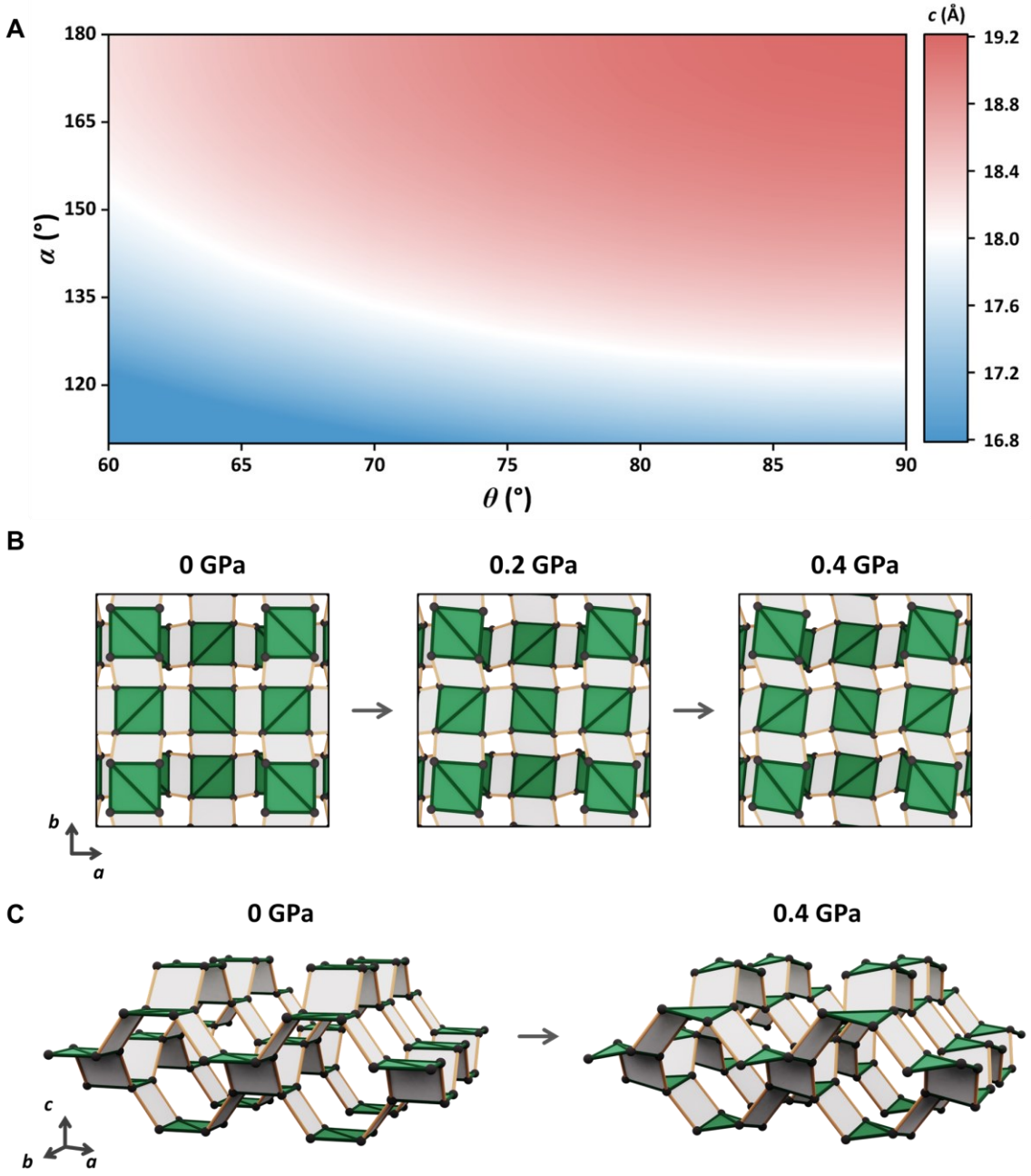

Figure 4. Mechanical behavior of gis-ZIF-1. (A) Contour map plotting calculated *c* parameters by the mathematical model. Representation of kirigamic ZIF mechanics based on HP-PXRD data in (B) the *ab* plane at 0 (left), 0.2 (middle) and 0.4 (right) GPa and (C) its side view, ranging from 0 (left) to 0.4 (right) GPa. Green and white tiles represent symmetrically equivalent 4MRs, connected by green and light-yellow edges (imidazolate sites and folding hinges) with Zn atoms (grey).

https://doi.org/10.26434/chemrxiv-2024-ffwgh-v2 **ORCID:** https://orcid.org/0000-0001-5123-418X Content not peer-reviewed by ChemRxiv. **License:** CC BY-NC 4.0

Kirigamic *lp*-to-*np* transition. We also investigated any structural changes within **gis**-ZIF-1 upon solvent-exchange process. After soaking the as-synthesized **gis**-ZIF-1 single-crystals in ethanol, the tetragonal **gis**-ZIF-1 structure was transformed to **gis**-ZIF-*np*, the orthorhombic narrow pore (*np*) phase in **gis** topology (Figure 5A), confirmed by SCXRD (Table S6). The **gis**-ZIF-*np* has the orthorhombic *P*nma space group symmetry. The unit cell contains 16 Zn sites (T sites, hereafter) and 32 Im sites (O sites, hereafter), the same as the tetragonal large pore (*lp*) **gis**-ZIF-1 (**gis**-ZIF-*lp*, hereafter). The unit cell volume of **gis**-ZIF-*np* is 4567.8(15) $Å^3$, about 30% smaller than that of **gis**-ZIF-*lp* at 300K.[29] To our surprise, this *lp*-to-*np* transformation is highly anisotropic, exemplified by *a* parameter from 18.450(3) Å to 11.701(2) Å and 20.133(4) Å, exhibiting 37% decrease and 9% increase, respectively, while *c* parameter from 19.494(4) Å to 19.390(4) Å indicating mere 0.5% decrease.

We further tested other solvents, e.g. DEF, DMF, DMA, MeOH, EtOH, THF, DCM, acetone and water, and without any solvents (after activating the sample). The cell parameters of these *lp* and *np* phases of **gis**-ZIFs are varied widely depending on the types of solvents (Figure S13A). When washing and exchanging the solvents of pristine crystals (**gis**-ZIF-*lp* phase) with amide solvents, PXRD patterns were well-maintained with slight shifts in reflections, matching with the ones in the previous reports.[29] However, for other solvents, e.g. MeOH, EtOH, THF, DCM, acetone and water, *lp*-to-*np* transition occurred, and no further structural transitions observed under thermal activation. Interestingly, only amide solvents with a dipole moment of 3.5 D or higher maintain the *lp* phase (Figure S13B).

Notably, **gis**-ZIF-*np* is the first orthorhombic **gis**-ZIF known to date, highly exceptional for **gis**-type framework, including zeolites (Table S7). In particular, the **gis**-ZIF-*np* structure has the lowest folding angle β among **gis**-type frameworks, even below 90° (Figure 5B, Table S8). This kirigamic *lp*-to-*np* transition resulted in a highly anisotropic structure, while other reported

https://doi.org/10.26434/chemrxiv-2024-ffwgh-v2 **ORCID:** https://orcid.org/0000-0001-5123-418X Content not peer-reviewed by ChemRxiv. **License:** CC BY-NC 4.0

gis-type frameworks belong to (pseudo-)tetragonal geometry (Figure 5C). This unique anisotropic transition was accompanied by the change of OTO angles, where the maximum angle is 123.7°. Such unusually high OTO angles found in **gis**-type ZIFs and zeolites, are the molecular origin for this *lp*-to-*np* transition (Table S9).

Based on these observations, we conclude that the flexible nature of **gis**-type ZIFs is originated from these folding angles between the kirigami building blocks, responsible for mechanical, and guest-induced movements, in stark contrast to **gis**-zeolites, where these zeolites did not show the change in folding angles (Figure 5D, Figure S14). Also, *lp*-to-*np* and its reverse *np*-to-*lp* transitions of **gis**-ZIFs are not possible by thermal and mechanical stimuli, but by guests (Table S6, Figure S15). In case of mechanical stimuli, **gis**-ZIF-*np* shows another type of phase transition, wherein the transition is partially reversible (Figure S16, Table S11).

https://doi.org/10.26434/chemrxiv-2024-ffwgh-v2 **ORCID:** https://orcid.org/0000-0001-5123-418X Content not peer-reviewed by ChemRxiv. **License:** CC BY-NC 4.0

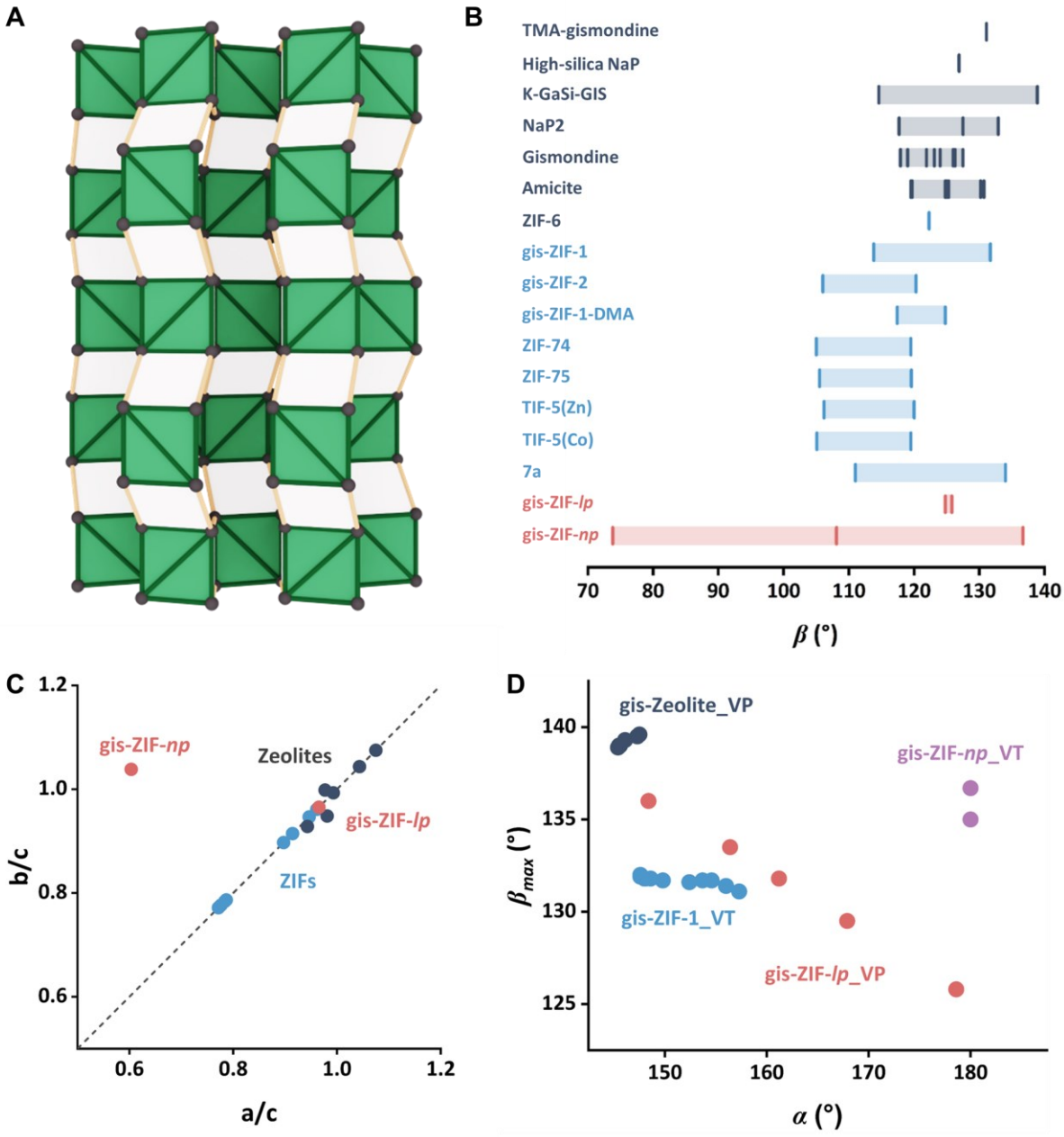

Figure 5. Structural characterization of gis-ZIF-*np*. (A) Kirigamic model of the single-crystal **gis**-ZIF-*np* structure viewing on (001) plane, and comparison of **gis**-type frameworks in terms of (B) folding angles and (C) cell parameters, wherein monoclinic structures are plotted as *a*/*b* and *c*/*b* instead of *a*/*c* and *b*/*c*, according to the direction of dcc units inside unit cell (see Table S7, S8). (D) Folding angles in **gis**-ZIFs and zeolites under thermal (VT) and mechanical (VP) stimuli (see Table S10). Green and white tiles represent symmetrically equivalent 4MRs, connected by green and light-yellow edges which represent imidazolate sites and folding hinges, with Zn atoms depicted in grey. Red, purple, blue, and navy colors denote the structures of this work (*lp* and *np*), ZIFs and zeolites, respectively.

https://doi.org/10.26434/chemrxiv-2024-ffwgh-v2 **ORCID:** https://orcid.org/0000-0001-5123-418X Content not peer-reviewed by ChemRxiv. **License:** CC BY-NC 4.0

Transformation of pore dimensionality resulting from kirigami mechanics. Thus far, we have demonstrated the folding mechanics of **gis**-ZIF-1 under mechanical stimuli and the solvent-induced *lp*-to-*np* transition. Subsequently, we shifted our focus from the framework itself to the pore structures generated by the kirigamic framework. As previously described, the **gis** topology possesses an underlying **dia** topology, known as a self-dual net.[37] Therefore, the pore structure of the **gis** topology exhibits a distorted **dia** network, where the maximal symmetry embedding of the **gis** topology is $I4_1$/amd, a maximal subgroup of *F*d-3m, the maximal symmetry embedding of the **dia** topology (Figure S17). This distortion results in the 2D pore structure of **gis**-ZIF-*lp*, resembling pipes in contact at perpendicular angles (Figure S18). Interestingly, the pore dimensionality transforms from 2D to 1D during the kirigamic *lp*-to-*np* transition, with the increase of pore apertures of from 5.9 Å to 6.7 Å for *lp* and *np* at 100K, respectively, confirmed by SCXRD data of this work and reported **gis**-ZIF-*lp* (Figure 6A).[29] By adjusting the dimensionality of the porous channels, the flow paths of adsorbed gases can be controlled in **gis**-ZIF-1, similar to manifolds, which are widely used as multi-point distribution platforms in water supply and sewage systems.[38] During this transformation of pore dimensionality, 4MR tiles exhibit rotational movement, acting like check valves found in conventional manifolds (Figure 6B). Furthermore, this fully connected and crystalline porous system can be considered a dimension-reduced version of the plumber's nightmare structure (Figure 6C).[39,40]

To utilize this unique adsorptive feature, we investigated the unfolding mechanics through gas adsorption experiments to assess its response to various gases, e.g. O_2, N_2 and CO_2 at 77K, 77K and 196K, respectively (Figure S19A). For the isotherms of these gases, stepwise adsorption and hysteresis phenomena were observed, known for the breathing transition of dynamic frameworks.[41] To confirm the structural transition, we matched the experimental pore

https://doi.org/10.26434/chemrxiv-2024-ffwgh-v2 **ORCID:** https://orcid.org/0000-0001-5123-418X Content not peer-reviewed by ChemRxiv. **License:** CC BY-NC 4.0

volume with the calculated one, simulated by using crystallographic data (Figure 6D, Table S12, S13). From the N_2 physisorption, the range of pore volume values is about 0.15–0.22 cm^3 g^{-1} and 0.56–0.62 cm^3 g^{-1}, for the first (*np*) and second (*lp*) phases, respectively. For O_2 and CO_2 isotherms, we also calculated the pore volume, and obtained similar values (Figure S19B, S19C, Table S14, S15). For **gis**-ZIF-*np* and *lp* structures, the ranges of simulated void fraction and pore volume values are 0.25–0.26 and 0.22–0.23 cm^3 g^{-1} (*np* phase) and 0.53–0.54 and 0.61–0.67 cm^3 g^{-1} (*lp* phase), respectively. Compared to these data, the range of experimental pore volume values is matched well with simulated values.

Guest-induced phase transitions are one of the well-established behaviours in flexible MOFs, accompanied by wine-rack[42] and accordion-like mechanism,[43] linker swing,[44] cage deformation,[45] and interpenetration sliding.[46] Notably, the kirigami mechanics shown here is newly found, strikingly different from the categories described above.[42–46]

https://doi.org/10.26434/chemrxiv-2024-ffwgh-v2 **ORCID:** https://orcid.org/0000-0001-5123-418X Content not peer-reviewed by ChemRxiv. **License:** CC BY-NC 4.0

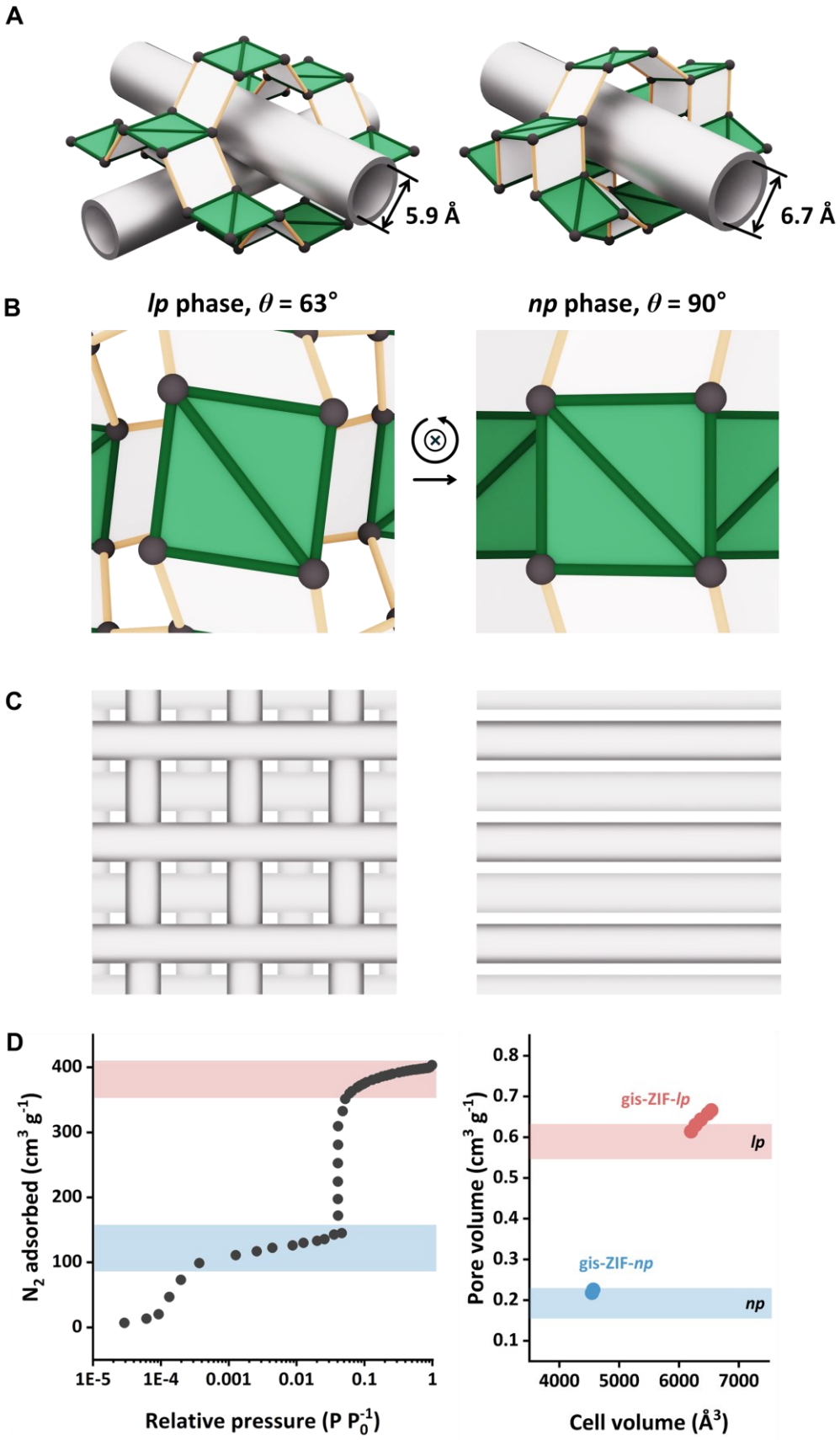

https://doi.org/10.26434/chemrxiv-2024-ffwgh-v2 **ORCID:** https://orcid.org/0000-0001-5123-418X Content not peer-reviewed by ChemRxiv. **License:** CC BY-NC 4.0

Figure 6. Pore structures of gis-ZIF-1. (A) Pore structures of **gis**-ZIF-*lp* (left) and *np* (right), represented by kirigamic framework (4MRs and Zn atoms represented by green and white tiles and grey balls) and channels (colored by white cylinders). (B) Comparison of 4MRs with different rotating angles based on single-crystal structures at 100K. During the single-crystal *np*-to-*lp* transition, 4MRs are rotating, ranging from 63˚(*lp*, left) to 90˚(*np*, right) of rotating angle θ, which resemble the role of check valves in the manifold. (C) Comparison of cylindrical pore paths between **gis**-ZIF-*lp* (left) and *np* (right). (D) Pore volume analysis in N_2 isotherm at 77K (left), and related correlation between cell volume and pore volume (right), where data points and colored regions correspond to crystallographic data and simulated pore volume, respectively.

https://doi.org/10.26434/chemrxiv-2024-ffwgh-v2 **ORCID:** https://orcid.org/0000-0001-5123-418X Content not peer-reviewed by ChemRxiv. **License:** CC BY-NC 4.0

DISCUSSION

In summary, we report **gis**-ZIF-1 as a kirigamic framework related to the DCS origami tessellation, assembled from 4MR components acting as rigid tiles, exhibiting 3D folding mechanics in the solid-state. Based on a simple mechanical model, we can now precisely predict the kirigamic movement in response to mechanical stimuli, especially how the folding of each 4MR tile influences unit cell compression. Surprisingly, by exchanging or removing the solvents, the tetragonal **gis**-ZIF, **gis**-ZIF-*lp*, is significantly folded and transformed to a unique orthorhombic structure, **gis**-ZIF-*np*. This kirigami mechanics involves a change in pore dimensionality, like a mechanical manifold with check valves to control the flow of fluids (Figure 7A). Resulting rod-packed pore networks resemble a dimensionality-reduced version of the plumber's nightmare structure, suggesting that kirigami mechanics can control complex pore networks (Figure 7B). That kirigamic 1D pore (*np*) unfolds back into the 2D *lp* structure upon gas adsorption.

Indeed, this **gis**-ZIF-1 belongs to the class of mechanical metamaterials based on a kirigami tessellation,[47] exhibiting programmable kinematics with stimuli-responsive features. Notably, recent studies have shown the interplay between the mechanical properties and various applications, as exemplified by energy harvesting, wherein the foldable metamaterial has a role of a triboelectric nanogenerator.[48] In our case, kirigami mechanics clearly correlates with solvent exchange and gas adsorption, presenting potential ways to utilize this molecular kirigami as a smart adsorbent. We expect that such efforts serve as a blueprint for deciphering solid-state kirigamic ZIFs at the molecular scale.

https://doi.org/10.26434/chemrxiv-2024-ffwgh-v2 **ORCID:** https://orcid.org/0000-0001-5123-418X Content not peer-reviewed by ChemRxiv. **License:** CC BY-NC 4.0

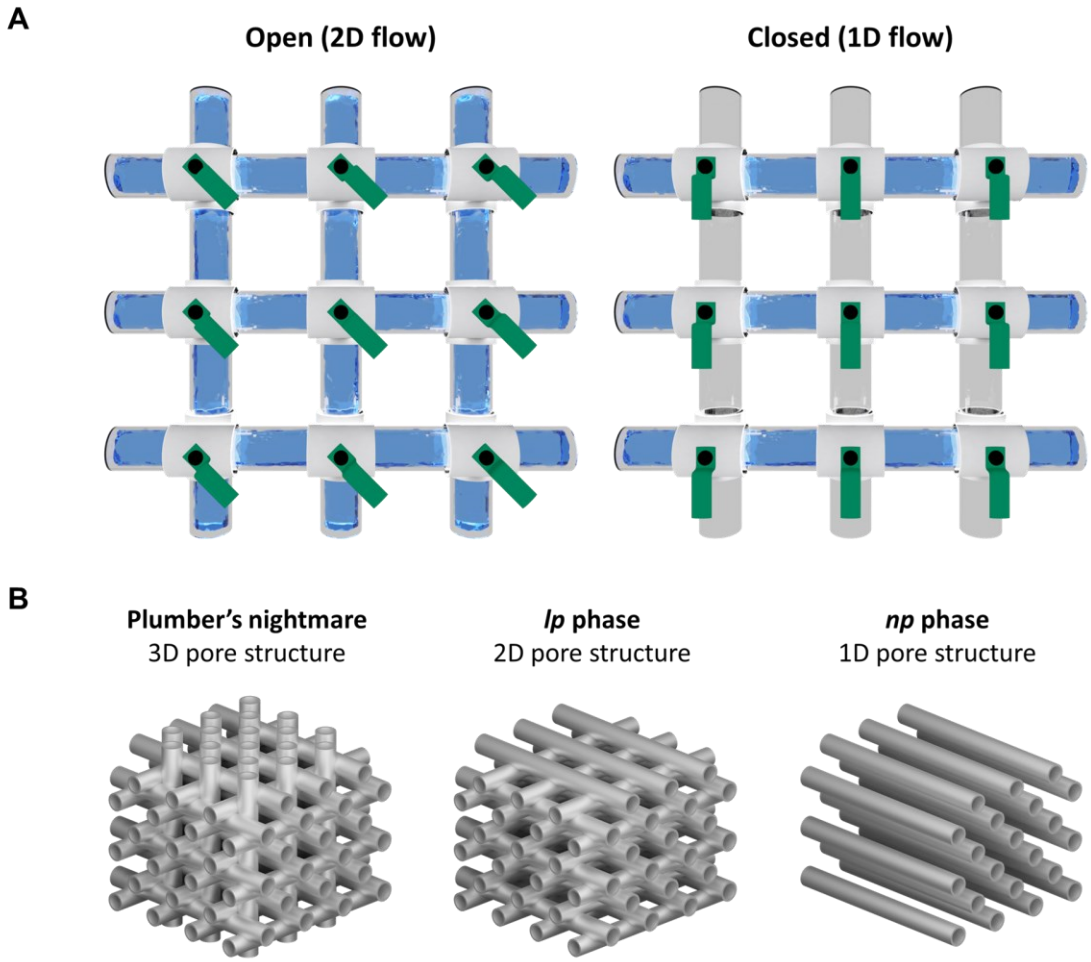

Figure 7. Scheme for mechanical analogues of the pore structures in gis-ZIF-1. (A) Scheme for the check valve-adapted conventional manifold. A manifold, a platform composed of pipes (represented as glass tubes) and check valves (represented as white caps and green valves with black joints), enables the directional control of the flow (represented as light blue fluid), where open (left) and closed (right) phases correspond to the 2D and 1D phase, respectively. (B) The plumber's nightmare structure (left) and rod-packed pore structures of *lp* (middle) and *np* phase (right) of **gis**-ZIF-1. The interconnected channels inside **gis**-ZIF-1 can be represented as the packing of porous rods, resembling a dimensionality-reduced version of the plumber's nightmare structure.

https://doi.org/10.26434/chemrxiv-2024-ffwgh-v2 **ORCID:** https://orcid.org/0000-0001-5123-418X Content not peer-reviewed by ChemRxiv. **License:** CC BY-NC 4.0

EXPERIMENTAL PROCEDURES

Synthesis and Characterization. All experimental procedures are available in the Article or Supplementary Information.

Powder X-ray diffraction (PXRD). X-ray powder diffraction data were collected on Bruker D2 PHASER diffractometer with Cu Kα radiation (λ=1.54184 Å) and at 2D beamline in Pohang Accelerator Laboratory (PAL) with synchrotron light source (λ=1.25 Å).

Temperature-dependent single-crystal X-ray diffraction (SCXRD). X-ray single-crystal diffraction data were collected at 2D beamline in Pohang Accelerator Laboratory (PAL) with synchrotron light source (λ=0.7 Å). Temperature-dependent SCXRD experiment was conducted from 100 K to 300 K. The crystallographic data was deposited in the Cambridge Crystallographic Data Centre (CCDC 2333190 and 2333191).

High-pressure synchrotron powder X-ray diffraction (HP-PXRD). The high-pressure powder diffraction experiments were conducted at Beamline BL9 of the DELTA Synchrotron Facility of TU Dortmund (Germany) (λ = 0.4592 Å) using the custom-built pressure jump set-up described elsewhere.[49,50] In short, samples were filled inside a glovebox into self-made capillaries made from Kapton tube, which are sealed at the bottom by epoxy. After filling of the ZIF into the capillary, the pressure transducer (Silicone Oil AP 100, Sigma Aldrich) was added. Subsequently, the capillary was centrifuged for two minutes (5000-10000 rpm) to push the pressure transducing medium to the bottom of the capillary, fully surrounding the sample. Before sealing the capillary by crimping with an aluminium seal, it was ensured that the capillary contained no gas bubbles. The closed capillaries were installed in a sample holder located in the high-pressure cell and submerged in a body of water. The water pressure inside

https://doi.org/10.26434/chemrxiv-2024-ffwgh-v2 **ORCID:** https://orcid.org/0000-0001-5123-418X Content not peer-reviewed by ChemRxiv. **License:** CC BY-NC 4.0

the measurement cell was adjusted via a mechanical pump and controlled via a manometer. The powder diffraction patterns were extracted from the 2D diffraction images collected with a MAR3450 detector using the 2D powder diffraction and processing tools of the DAWN software package.[51,52]

Structural refinement and analysis from PXRD data. Entire PXRD patterns were fitted according to the Le Bail method,[53] and Rietveld refinement[54] was conducted for selected data sets.

Gas adsorption. Gas adsorption analysis was performed on BELSORP-max (BEL Japan, Inc.) instrument.

Synthesis of gis-ZIF-*lp*. **gis**-ZIF-*lp* was synthesized following a reported method.[29] To prepare the stock solution, Zinc trifluoromethanesulfonate (2.908 g, 8 mmol) and imidazole (2.18 g, 32 mmol) were separately dissolved in 40 mL of diethylformamide (DEF). Subsequently, 2 mL of the zinc trifluoromethanesulfonate stock solution and 1 mL of the imidazole stock solution were combined in a 10 mL vial. Then, an additional 1 mL of DEF and 30 μL of ethylenediamine (27 mg, 0.45 mmol) were added to the same vial. The mixture was heated at 90 ℃ for 48 hours. After the reaction, the resulting colorless crystals were collected and washed with DEF.

Preparation of gis-ZIF-*np*. Prepared **gis**-ZIF-*lp* powder crystals were washed with EtOH, for 4 times in 2 days. After the solvent-exchange, the resulting colorless crystals were collected. To measure PXRD, EtOH-soaked **gis**-ZIF-*np* crystals were activated about 12 hours at 120 °C.

RESOURCE AVAILABILITY

Lead Contact

https://doi.org/10.26434/chemrxiv-2024-ffwgh-v2 **ORCID:** https://orcid.org/0000-0001-5123-418X Content not peer-reviewed by ChemRxiv. **License:** CC BY-NC 4.0

Further information and requests for resources should be directed to and will be fulfilled by the lead contact, Wonyoung Choe (choe@unist.ac.kr)

Materials Availability

This study did not generate new reagents.

Data and Code Availability

All data are available in the Article or Supplementary Information. Any additional data related to this paper can be obtained from the lead contact upon request. This study did not generate/analyze code.

AUTHOR INFORMATION

Corresponding Authors

E-mail: *andreas.schneemann@tu-dresden.de, **choe@unist.ac.kr

Author contributions

Conceptualization, J.N. and W.C.; Methodology, J.N., A.S. and W.C.; Crystal structure analysis, J.N. and W.C.; High-pressure experiment, L.A., J.G., W.X., S.H. and A.S.; Gas adsorption analysis, J.N., H.O., H.L., and H.R.M. Writing – Original draft, Review & Editing, J.N., A.S. and W.C. Funding acquisition, W.C.

DECLARATION OF INTERESTS

The authors declare no competing interests.

ACKNOWLEDGEMENTS

https://doi.org/10.26434/chemrxiv-2024-ffwgh-v2 **ORCID:** https://orcid.org/0000-0001-5123-418X Content not peer-reviewed by ChemRxiv. **License:** CC BY-NC 4.0

This work was supported by the National Research Foundation (NRF) of Korea (NRF-2020R1A2C3008226, NRF-2021M3I3A1084909, and RS-2023-00279793), and the Carbon Neutral Institute Research Fund (Project # 1.230051.01, 1.230069.01) of Ulsan National Institute of Science and Technology (UNIST). We acknowledge the Pohang Accelerator Laboratory (PAL) for 2D beamline use (2023-2nd-2D-030). These authors gratefully acknowledge DELTA for providing synchrotron radiation beamtime at beamline BL9 and Dr. Michael Paulus and Dr. Christian Sternemann for support during experiments. A.S. gratefully acknowledges the Fonds der chemischen Industrie for a Liebig Fellowship.

https://doi.org/10.26434/chemrxiv-2024-ffwgh-v2 **ORCID:** https://orcid.org/0000-0001-5123-418X Content not peer-reviewed by ChemRxiv. **License:** CC BY-NC 4.0

References

(1) Badalucco, L. *Kirigami: The Art of 3-Dimensional Paper Cutting*; Sterling Publishing, 2001.

(2) Collins, G. P. Kirigami and Technology Cut a Fine Figure, Together. *Proc. Natl. Acad. Sci.* **2016**, *113* (2), 240–241. https://doi.org/10.1073/pnas.1523311113.

(3) An, N.; Domel, A. G.; Zhou, J.; Rafsanjani, A.; Bertoldi, K. Programmable Hierarchical Kirigami. *Adv. Funct. Mater.* **2020**, *30* (6), 1906711. https://doi.org/10.1002/adfm.201906711.

(4) Tang, Y.; Lin, G.; Yang, S.; Yi, Y. K.; Kamien, R. D.; Yin, J. Programmable Kiri-Kirigami Metamaterials. *Adv. Mater.* **2017**, *29* (10), 1604262. https://doi.org/10.1002/adma.201604262.

(5) Choi, G. P. T.; Dudte, L. H.; Mahadevan, L. Programming Shape Using Kirigami Tessellations. *Nat. Mater.* **2019**, *18* (9), 999–1004. https://doi.org/10.1038/s41563-019-0452-y.

(6) Li, Y.; Zhang, Q.; Hong, Y.; Yin, J. 3D Transformable Modular Kirigami Based Programmable Metamaterials. *Adv. Funct. Mater.* **2021**, *31* (43), 2105641. https://doi.org/10.1002/adfm.202105641.

(7) Jiang, S.; Liu, J.; Xiong, W.; Yang, Z.; Yin, L.; Li, K.; Huang, Y. A Snakeskin-Inspired, Soft-Hinge Kirigami Metamaterial for Self-Adaptive Conformal Electronic Armor. *Adv. Mater.* **2022**, *34* (31), 2204091. https://doi.org/10.1002/adma.202204091.

(8) Zhang, H.; Paik, J. Kirigami Design and Modeling for Strong, Lightweight Metamaterials. *Adv. Funct. Mater.* **2022**, *32* (21), 2107401. https://doi.org/10.1002/adfm.202107401.

(9) Zhai, Z.; Wu, L.; Jiang, H. Mechanical Metamaterials Based on Origami and Kirigami. *Appl. Phys. Rev.* **2021**, *8* (4), 041319. https://doi.org/10.1063/5.0051088.

(10) He, Q.; Yin, R.; Hua, Y.; Jiao, W.; Mo, C.; Shu, H.; Raney, J. R. A Modular Strategy for Distributed, Embodied Control of Electronics-Free Soft Robots. *Sci. Adv.* **2023**, *9* (27), eade9247. https://doi.org/10.1126/sciadv.ade9247.

(11) Meng, K.; Xiao, X.; Liu, Z.; Shen, S.; Tat, T.; Wang, Z.; Lu, C.; Ding, W.; He, X.; Yang, J.; Chen, J. Kirigami-Inspired Pressure Sensors for Wearable Dynamic Cardiovascular Monitoring. *Adv. Mater.* **2022**, *34* (36), 2202478. https://doi.org/10.1002/adma.202202478.

(12) Zhang, X.; Ma, J.; Li, M.; You, Z.; Wang, X.; Luo, Y.; Ma, K.; Chen, Y. Kirigami-Based Metastructures with Programmable Multistability. *Proc. Natl. Acad. Sci.* **2022**, *119* (11), e2117649119. https://doi.org/10.1073/pnas.2117649119.

(13) Morikawa, Y.; Yamagiwa, S.; Sawahata, H.; Numano, R.; Koida, K.; Kawano, T. Donut-Shaped Stretchable Kirigami: Enabling Electronics to Integrate with the Deformable Muscle. *Adv. Healthc. Mater.* **2019**, *8* (23), 1900939. https://doi.org/10.1002/adhm.201900939.

(14) Zheng, Y.; Chen, K.; Yang, W.; Wu, L.; Qu, K.; Zhao, J.; Jiang, T.; Feng, Y. Kirigami Reconfigurable Gradient Metasurface. *Adv. Funct. Mater.* **2022**, *32* (5), 2107699. https://doi.org/10.1002/adfm.202107699.

(15) Jin, E.; Lee, I. S.; Yang, D. C.; Moon, D.; Nam, J.; Cho, H.; Kang, E.; Lee, J.; Noh, H.-J.; Min, S. K.; Choe, W. Origamic Metal-Organic Framework toward Mechanical Metamaterial. *Nat. Commun.* **2023**, *14* (1), 7938. https://doi.org/10.1038/s41467-023-43647-8.

(16) Sun, Y.; Ye, W.; Chen, Y.; Fan, W.; Feng, J.; Sareh, P. Geometric Design Classification of Kirigami-Inspired Metastructures and Metamaterials. *Structures* **2021**, *33*, 3633–3643. https://doi.org/10.1016/j.istruc.2021.06.072.

(17) Castle, T.; Sussman, D. M.; Tanis, M.; Kamien, R. D. Additive Lattice Kirigami. *Sci. Adv.* **2016**, *2* (9), e1601258. https://doi.org/10.1126/sciadv.1601258.

(18) Phon, R.; Jeong, H.; Lim, S. Rotational Kirigami Tessellation Metasurface for Tunable Chirality. *Adv. Mater. Technol.* **2022**, *7* (10), 2101706. https://doi.org/10.1002/admt.202101706.

(19) Dang, X.; Feng, F.; Duan, H.; Wang, J. Theorem for the Design of Deployable Kirigami Tessellations with Different Topologies. *Phys. Rev. E* **2021**, *104* (5), 055006. https://doi.org/10.1103/PhysRevE.104.055006.

(20) Dang, X.; Feng, F.; Duan, H.; Wang, J. Theorem on the Compatibility of Spherical Kirigami Tessellations. *Phys. Rev. Lett.* **2022**, *128* (3), 035501. https://doi.org/10.1103/PhysRevLett.128.035501.

(21) Norton, R. L. *Design of Machinery: An Introduction to the Synthesis and Analysis of Mechanisms and Machines*; Mcgraw-Hill College, 2003.

(22) Nam, J.; Kim, S.; Jin, E.; Lee, S.; Cho, H. J.; Min, S. K.; Choe, W. Zeolitic Imidazolate Frameworks as Transformable Mechanical Nanomachines.

(23) McCarthy, J. M.; Soh, G. S. *Geometric Design of Linkages (Interdisciplinary Applied Mathematics, 11)*; Springer, 2010.

https://doi.org/10.26434/chemrxiv-2024-ffwgh-v2 **ORCID:** https://orcid.org/0000-0001-5123-418X Content not peer-reviewed by ChemRxiv. **License:** CC BY-NC 4.0

(24) Zhang, X.; Medina, L.; Cai, H.; Aksyuk, V.; Espinosa, H. D.; Lopez, D. Kirigami Engineering—Nanoscale Structures Exhibiting a Range of Controllable 3D Configurations. *Adv. Mater.* **2021**, *33* (5), 2005275. https://doi.org/10.1002/adma.202005275.
(25) Wang, H.; Pei, X.; Kalmutzki, M. J.; Yang, J.; Yaghi, O. M. Large Cages of Zeolitic Imidazolate Frameworks. *Acc. Chem. Res.* **2022**, *55* (5), 707–721. https://doi.org/10.1021/acs.accounts.1c00740.
(26) Park, K. S.; Ni, Z.; Côté, A. P.; Choi, J. Y.; Huang, R.; Uribe-Romo, F. J.; Chae, H. K.; O'Keeffe, M.; Yaghi, O. M. Exceptional Chemical and Thermal Stability of Zeolitic Imidazolate Frameworks. *Proc. Natl. Acad. Sci.* **2006**, *103* (27), 10186–10191. https://doi.org/10.1073/pnas.0602439103.
(27) Noh, K.; Lee, J.; Kim, J. Compositions and Structures of Zeolitic Imidazolate Frameworks. *Isr. J. Chem.* **2018**, *58* (9–10), 1075–1088. https://doi.org/10.1002/ijch.201800107.
(28) Iacomi, P.; Maurin, G. ResponZIF Structures: Zeolitic Imidazolate Frameworks as Stimuli-Responsive Materials. *ACS Appl. Mater. Interfaces* **2021**, *13* (43), 50602–50642. https://doi.org/10.1021/acsami.1c12403.
(29) Nam, J.; Kim, S.; Jin, E.; Lee, S.; Cho, H. J.; Min, S. K.; Choe, W. Zeolitic Imidazolate Frameworks as Solid-State Nanomachines. *Angew. Chem. Int. Ed.* **2024**, e202404061. https://doi.org/10.1002/anie.202404061.
(30) Gao, M.; Huang, R.-K.; Zheng, B.; Wang, P.; Shi, Q.; Zhang, W.-X.; Dong, J. Large Breathing Effect in ZIF-65(Zn) with Expansion and Contraction of the SOD Cage. *Nat. Commun.* **2022**, *13* (1), 4569. https://doi.org/10.1038/s41467-022-32332-x.
(31) Sartbaeva, A.; Wells, S. A.; Treacy, M. M. J.; Thorpe, M. F. The Flexibility Window in Zeolites. *Nat. Mater.* **2006**, *5* (12), 962–965. https://doi.org/10.1038/nmat1784.
(32) Wharmby, M. T.; Henke, S.; Bennett, T. D.; Bajpe, S. R.; Schwedler, I.; Thompson, S. P.; Gozzo, F.; Simoncic, P.; Mellot-Draznieks, C.; Tao, H.; Yue, Y.; Cheetham, A. K. Extreme Flexibility in a Zeolitic Imidazolate Framework: Porous to Dense Phase Transition in Desolvated ZIF-4. *Angew. Chem. Int. Ed.* **2015**, *54* (22), 6447–6451. https://doi.org/10.1002/anie.201410167.
(33) Silverberg, J. L.; Na, J.-H.; Evans, A. A.; Liu, B.; Hull, T. C.; Santangelo, C. D.; Lang, R. J.; Hayward, R. C.; Cohen, I. Origami Structures with a Critical Transition to Bistability Arising from Hidden Degrees of Freedom. *Nat. Mater.* **2015**, *14*.
(34) Guo, P.; Yan, N.; Wang, L.; Zou, X. Database Mining of Zeolite Structures. *Cryst. Growth Des.* **2017**, *17* (12), 6821–6835. https://doi.org/10.1021/acs.cgd.7b01410.
(35) Song, J.; Pallach, R.; Frentzel-Beyme, L.; Kolodzeiski, P.; Kieslich, G.; Vervoorts, P.; Hobday, C. L.; Henke, S. Tuning the High-Pressure Phase Behaviour of Highly Compressible Zeolitic Imidazolate Frameworks: From Discontinuous to Continuous Pore Closure by Linker Substitution. *Angew. Chem. Int. Ed.* **2022**, *61* (21), e202117565. https://doi.org/10.1002/anie.202117565.
(36) Vervoorts, P.; Stebani, J.; Méndez, A. S. J.; Kieslich, G. Structural Chemistry of Metal–Organic Frameworks under Hydrostatic Pressures. *ACS Mater. Lett.* **2021**, *3* (12), 1635–1651. https://doi.org/10.1021/acsmaterialslett.1c00250.
(37) Bonneau, C.; Delgado-Friedrichs, O.; O'Keeffe, M.; Yaghi, O. M. Three-Periodic Nets and Tilings: Minimal Nets. *Acta Crystallogr. A* **2004**, *60* (6), 517–520. https://doi.org/10.1107/S0108767304015442.
(38) Wang, Y.; Duan, M.; Xu, M.; Wang, D.; Feng, W. A Mathematical Model for Subsea Wells Partition in the Layout of Cluster Manifolds. *Appl. Ocean Res.* **2012**, *36*, 26–35. https://doi.org/10.1016/j.apor.2012.02.002.
(39) Lee, H.; Kwon, S.; Min, J.; Jin, S.-M.; Hwang, J. H.; Lee, E.; Lee, W. B.; Park, M. J. Thermodynamically Stable Plumber's Nightmare Structures in Block Copolymers. *Science* **2024**, *383* (6678), 70–76. https://doi.org/10.1126/science.adh0483.
(40) Jain, A.; Toombes, G. E. S.; Hall, L. M.; Mahajan, S.; Garcia, C. B. W.; Probst, W.; Gruner, S. M.; Wiesner, U. Direct Access to Bicontinuous Skeletal Inorganic Plumber's Nightmare Networks from Block Copolymers. *Angew. Chem. Int. Ed.* **2005**, *44* (8), 1226–1229. https://doi.org/10.1002/anie.200461156.
(41) Evans, J. D.; Bon, V.; Senkovska, I.; Lee, H.-C.; Kaskel, S. Four-Dimensional Metal-Organic Frameworks. *Nat. Commun.* **2020**, *11* (1), 2690. https://doi.org/10.1038/s41467-020-16527-8.
(42) Kim, J. Y.; Park, J.; Ha, J.; Jung, M.; Wallacher, D.; Franz, A.; Balderas-Xicohténcatl, R.; Hirscher, M.; Kang, S. G.; Park, J. T.; Oh, I. H.; Moon, H. R.; Oh, H. Specific Isotope-Responsive Breathing

https://doi.org/10.26434/chemrxiv-2024-ffwgh-v2 **ORCID:** https://orcid.org/0000-0001-5123-418X Content not peer-reviewed by ChemRxiv. **License:** CC BY-NC 4.0

Transition in Flexible Metal–Organic Frameworks. *J. Am. Chem. Soc.* **2020**, *142* (31), 13278–13282. https://doi.org/10.1021/jacs.0c04277.

(43) Li, X.-L.; Liu, G.-Z.; Xin, L.-Y.; Wang, L.-Y. A Novel Metal–Organic Framework Displaying Reversibly Shrinking and Expanding Pore Modulation. *CrystEngComm* **2012**, *14* (18), 5757. https://doi.org/10.1039/c2ce25715g.

(44) Koutsianos, A.; Pallach, R.; Frentzel-Beyme, L.; Das, C.; Paulus, M.; Sternemann, C.; Henke, S. Breathing Porous Liquids Based on Responsive Metal-Organic Framework Particles. *Nat. Commun.* **2023**, *14* (1), 4200. https://doi.org/10.1038/s41467-023-39887-3.

(45) Gao, M.; Huang, R.-K.; Zheng, B.; Wang, P.; Shi, Q.; Zhang, W.-X.; Dong, J. Large Breathing Effect in ZIF-65(Zn) with Expansion and Contraction of the SOD Cage. *Nat. Commun.* **2022**, *13* (1), 4569. https://doi.org/10.1038/s41467-022-32332-x.

(46) Zhu, Y.; Cai, J.; Xu, L.; Li, G.; Liu, Y. Two Robust Isoreticular Metal–Organic Frameworks with Different Interpenetration Degrees Exhibiting Disparate Breathing Behaviors. *Inorg. Chem.* **2022**, *61* (28), 10957–10964. https://doi.org/10.1021/acs.inorgchem.2c01545.

(47) Jiao, P.; Mueller, J.; Raney, J. R.; Zheng, X.; Alavi, A. H. Mechanical Metamaterials and Beyond. *Nat. Commun.* **2023**, *14* (1), 6004. https://doi.org/10.1038/s41467-023-41679-8.

(48) Zhang, H.; Yang, C.; Yu, Y.; Zhou, Y.; Quan, L.; Dong, S.; Luo, J. Origami-Tessellation-Based Triboelectric Nanogenerator for Energy Harvesting with Application in Road Pavement. *Nano Energy* **2020**, *78*, 105177. https://doi.org/10.1016/j.nanoen.2020.105177.

(49) Krywka, C.; Sternemann, C.; Paulus, M.; Javid, N.; Winter, R.; Al-Sawalmih, A.; Yi, S.; Raabe, D.; Tolan, M. The Small-Angle and Wide-Angle X-Ray Scattering Set-up at Beamline BL9 of DELTA. *J. Synchrotron Radiat.* **2007**, *14* (3), 244–251. https://doi.org/10.1107/S0909049507009727.

(50) Frentzel-Beyme, L.; Kolodzeiski, P.; Terlinden, K.; Henke, S. Microporous, Crystalline, and Water-Processable Framework Materials of Organic Amphiphile Salts. *Adv. Funct. Mater.* **2023**, *33* (36), 2302033. https://doi.org/10.1002/adfm.202302033.

(51) Filik, J.; Ashton, A. W.; Chang, P. C. Y.; Chater, P. A.; Day, S. J.; Drakopoulos, M.; Gerring, M. W.; Hart, M. L.; Magdysyuk, O. V.; Michalik, S.; Smith, A.; Tang, C. C.; Terrill, N. J.; Wharmby, M. T.; Wilhelm, H. Processing Two-Dimensional X-Ray Diffraction and Small-Angle Scattering Data in *DAWN 2*. *J. Appl. Crystallogr.* **2017**, *50* (3), 959–966. https://doi.org/10.1107/S1600576717004708.

(52) Basham, M.; Filik, J.; Wharmby, M. T.; Chang, P. C. Y.; El Kassaby, B.; Gerring, M.; Aishima, J.; Levik, K.; Pulford, B. C. A.; Sikharulidze, I.; Sneddon, D.; Webber, M.; Dhesi, S. S.; Maccherozzi, F.; Svensson, O.; Brockhauser, S.; Náray, G.; Ashton, A. W. *Data Analysis WorkbeNch* (*DAWN*). *J. Synchrotron Radiat.* **2015**, *22* (3), 853–858. https://doi.org/10.1107/S1600577515002283.

(53) Le Bail, A. Whole Powder Pattern Decomposition Methods and Applications: A Retrospection. *Powder Diffr.* **2005**, *20* (4), 316–326. https://doi.org/10.1154/1.2135315.

(54) Stinton, G. W.; Evans, J. S. O. Parametric Rietveld Refinement. **2007**.

https://doi.org/10.26434/chemrxiv-2024-ffwgh-v2 **ORCID:** https://orcid.org/0000-0001-5123-418X Content not peer-reviewed by ChemRxiv. **License:** CC BY-NC 4.0

Entry for the Table of Contents

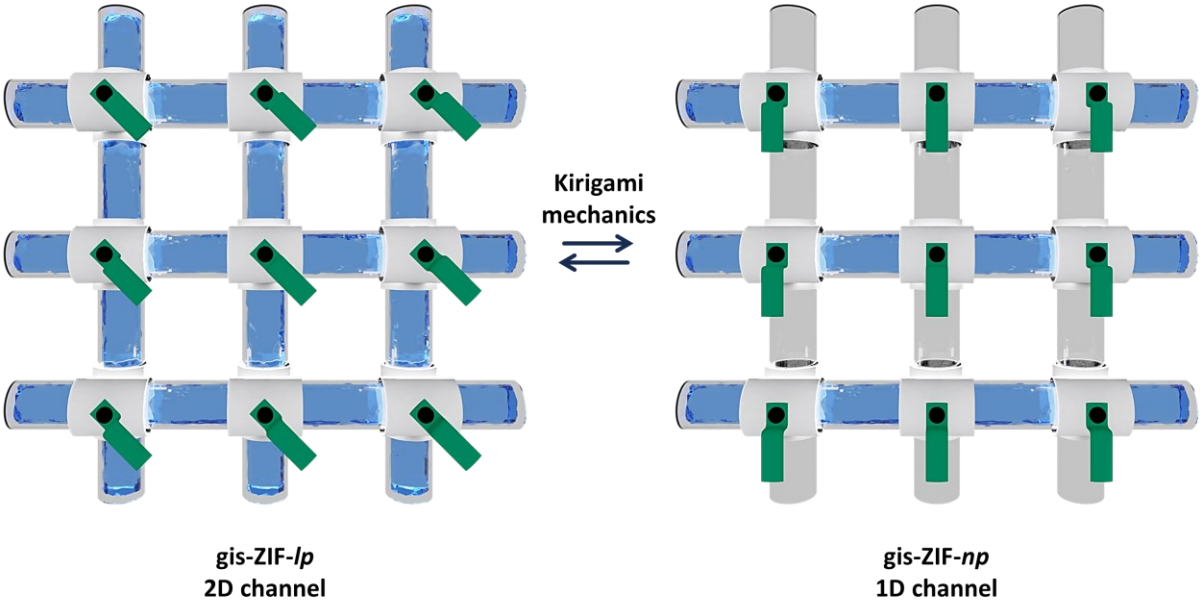

https://doi.org/10.26434/chemrxiv-2024-ffwgh-v2 **ORCID:** https://orcid.org/0000-0001-5123-418X Content not peer-reviewed by ChemRxiv. **License:** CC BY-NC 4.0